Stability error budget for an aggressive coronagraph on a 3.8 m telescope

Stuart B. Shaklan[1], Luis Marchen, John Krist, Mayer Rud
Jet Propulsion Laboratory, California Institute of Technology, 4800 Oak Grove Dr., Pasadena, CA 91109

ABSTRACT

We evaluate in detail the stability requirements for a band-limited coronagraph with an inner working angle as small as 2 λ/D coupled to an off-axis, 3.8-m diameter telescope. We have updated our methodologies since presenting a stability error budget for the Terrestrial Planet Finder Coronagraph mission that worked at 4 λ/D and employed an 8th-order mask to reduce aberration sensitivities. In the previous work, we determined the tolerances relative to the total light leaking through the coronagraph. Now, we separate the light into a radial component, which is readily separable from a planet signal, and an azimuthal component, which is easily confused with a planet signal. In the current study, throughput considerations require a 4th-order coronagraph. This, combined with the more aggressive working angle, places extraordinarily tight requirements on wavefront stability and opto-mechanical stability. We find that the requirements are driven mainly by coma that leaks around the coronagraph mask and mimics the localized signal of a planet, and pointing errors that scatter light into the background, decreasing SNR. We also show how the requirements would be relaxed if a low-order aberration detection system could be employed.

Keywords: Coronagraphy, high contrast imaging, error budget

1. INTRODUCTION

The search for earth-like exoplanets is one of NASA's key strategic goals[1] and is a high priority in the National Academy of Sciences Astro 2010: Astronomy and Astrophysics Decadal Survey.[2] The most thoroughly studied concept to date is the Terrestrial Planet Finder Coronagraph, TPF-C, an 8x3.5 m deployed, thermally stabilized telescope with a coronagraph forming high contrast images at an inner working angle (IWA) as close as 50 milli-arcsec (mas) from the image of a nearby, bright star.[3] In 2009, the Astrophysics Strategic Mission Concept Studies (ASMCS) addressed a range of telescope and instrument designs, from 1.5 m class apertures with more aggressive coronagraphs (ACCESS,[4,5] PECO,[6] EPIC[7]), to multi-aperture nullers (DaVINCI[8]), to 8-16 m class monolithic and segmented apertures (ATLAST[9]). More recently, the Decadal report called for a 4-m class aperture with a coronagraph or starshade to work in conjunction with an astrophysics mission. The starshade approach has been studied in the ASMCS s studies of THEIA[10] and New Worlds Observer.[11]

In this work we present the stability error budget for a 3.8 m telescope with an aggressive coronagraph having an IWA comparable to that of TPF-C. In a companion paper, we present an error budget for a 3.8 m telescope with a starshade.[12] Our coronagraph stability contrast error budget (CEB) is set up in an excel spreadsheet backed by layers of Visual Basic automation code and built on optical sensitivity matrices calculated from optical ray trace and diffraction codes. The error budget follows the overall approach outlined in Shaklan *et al* 2005[13] and utilizes updated versions of the automation features described in Marchen & Shaklan.[14] We have modified the combination of thermal and jitter terms to better represent the expected systematic noise floor. Treatment of scatter in the image plane is now similar the approach used to evaluate starshade scatter.[15]

[1] E-mail: Stuart.b.shaklan@jpl.nasa.gov; Phone: 818-354-0105

As in our earlier work, the error budget is based on a 'set and forget' approach where a dark hole is assumed to be set to a given level of performance at the beginning of an observation. It degrades over time as thermal changes and mechanical jitter move and bend optics and warp the wavefront. The stability requirements describe how much thermal deformation and jitter motion is allowed before the scattered light level in the dark hole exceeds the allowable level. But in the present work we also consider the presence of a low-order wavefront sensor (LOWFS)[16] and low-order wavefront control system that allows us to monitor and control several key low order Zernike modes.

The following section describes the CEB architecture and the specific models used to compute sensitivity matrices. Section 3 addresses the combination of scatter terms to arrive at the systematic and photometric noise floors. In Section 4 we update changes to the error budget structure and functionality since our previous report.[14] Section 5 then provides the detailed stability requirements for several coronagraph configurations and shows how the requirements change if an ideal LOWFS is included in the system.

2. MODELS

The CEB computes the image plane systematic and photometric noise floors for thermally- and dynamically-induced changes to the state of the instrument. The metric used is the instrument contrast, defined as the ratio of starlight scattered into a diffraction-limited resolution spot and normalized by the coronagraph mask throughput, to the peak of the starlight without the mask in place. See Green & Shaklan[17] for a more rigorous definition.

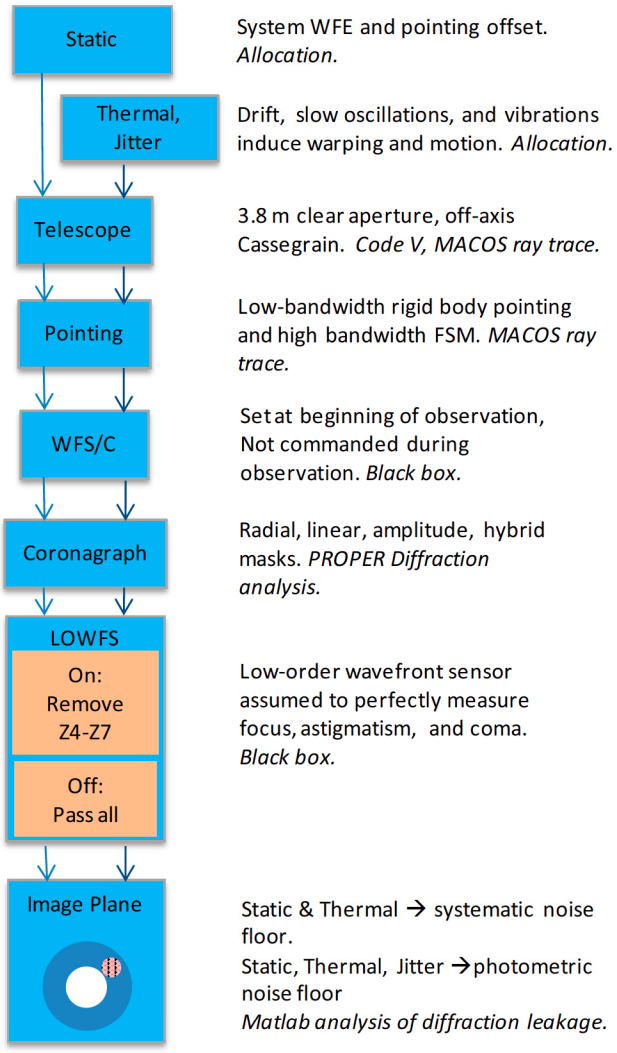

Figure 1. Block diagram of the model.

The contrast is evaluated using the models whose main building blocks are shown in Figure 1. The telescope, pointing, and wavefront control, systems form a pristine image of a star onto a coronagraphic mask. The combination of the mask and a Lyot stop filter out the ideal beam diffraction resulting in a 'dark hole' around the location where the stellar image would appear.[18] The achievable contrast in the dark hole is a function of the ability to measure and control the complex wavefront. In this work, we treat the wavefront control system as a black-box that achieves an initial contrast and is held perfectly stable during the observation. We assume it achieves the dark hole over the required bandwidth, at the required IWA. We then evaluate the contrast in the dark hole as the system is deformed by thermal and pointing drifts, and by jitter.

Two optical programs are used to perform ray tracing and diffraction analysis. We use the JPL-developed MACOS[19] program to determine the sensitivity of chief ray position and wavefront aberration content to the motion of any optic in the system as well as to rigid-body pointing of the whole system. Through a Matlab interface, the sensitivity matrices are built one degree-of-freedom (DoF) at a time. MACOS reads a converted optical prescription originally generated by either Zemax or CodeV.

We use the JPL-developed PROPER[20] diffraction analysis package to compute the leakage of aberrated starlight through the coronagraph. We assume a uniform beam and evaluate the fields that appear in the image plane when Zernike modes 2 through 13 (Noll ordered[21]) are incident on the mask. The MACOS aberration sensitivity matrices dA/dx, where dx is

an allocated mechanical DoF in the system, determine the change in aberration *dA* to be evaluated by the PROPER-derived contrast sensitivities *C(A)* to determine the contrast leakage for all DoFs in the system. The contrast calculations are discussed in more detail in section 2.3.

2.1 Telescope and Instrument

The telescope is an off-axis Cassegrain with a 3.8 m clear aperture (fig. 1). Studies have shown that this is approximately the largest aperture that can be realistically accommodated in existing (e.g. Atlas V) launch fairings.[22] An off-axis design is necessary to provide an unobscured aperture for the coronagraph; apertures with a central obscuration require low-throughput Lyot stops that are not suitable for exo-earth imaging.

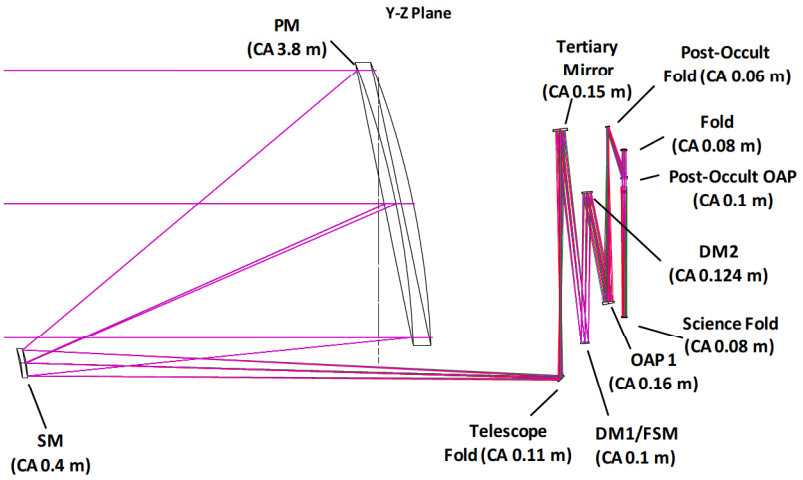

Figure 2. Telescope and instrument layout.

The separation between the primary and secondary mirrors is 5.5 m (vertex to vertex). The THEIA[10] Astrophysics Strategic Mission Concept Study (ASMCS) showed that this is the maximum length of the telescope consistent with the fairing length and the stack height required for a wide-field general astrophysics camera,[23] a deep UV spectrometer,[24] and the spacecraft. Table 1 shows the telescope design parameters. In designing the telescope we also considered a Gregorian design but this required a faster primary mirror that would likely have tighter stability tolerances in addition to being more difficult to manufacture.

Table 1. Telescope Design Parameters

Design	Cassegrain
PM Diam	4 m
PM Clear Ap.	3.8 m
PM-SM separation	5.5 m along Z axis
PM ROC, conic	12.155 m, k=-1
PM Parent f/no	F/0.69
PM Angle of Incidence	2.8-19.9 deg
Off-axis displacement	2.5 m
SM ROC, conic	1.237 m, k=-1.3057

The coronagraph instrument is based on the ACCESS[5,6] design. The beam is folded at a flat upstream of the f/24 Cassegrain focus. This is followed by an off-axis parabola (OAP, labeled Tertiary Mirror in fig. 1). A pupil image is formed at deformable mirror DM1, which is then followed by DM2. The sequential arrangement of DMs is used for both phase control and broad-band amplitude control.[25]. A second OAP forms an f/21 image where the coronagraph mask is placed. This is followed by a fold mirror and the Lyot Stop. Our contrast modeling includes the primary mirror (PM), secondary mirror (SM), and the optics up to the final OAP before the coronagraph mask. After the mask, most of the starlight is removed and the sensitivity to motion is greatly reduced.

2.2 Coronagraph Mask

Presently the CEB includes models of 4th order hybrid[26] and amplitude-only band-limited Lyot coronagraphs for this work. Hybrid masks enable smaller IWA and with larger Lyot stops than pure amplitude masks. We use radial and linear 1 - sinc-squared profiles because they provide superior image-plane coverage (but with slightly smaller Lyot throughput) than cosine masks. Pure amplitude 1-sinc^2 masks have been used to achieve the best contrasts to date in the High Contrast Imaging Testbed (HCIT),[27] while hybrid 1-sinc^2 masks have been used in the laboratory to achieve high contrast at 3 λ/D.[28] Green & Shaklan[17] showed that 1-sinc^2 amplitude masks had very similar aberration sensitivity as 1-cos and 1-sinc masks. Thus our CEB is representative of the performance of any number of 4th-order solutions.

The equations for the hybrid radial masks are[26]:

$$A^R(x) = 1 - \mathrm{sinc}^2(\pi r/w) \quad (1)$$

$$A^I(x) = 0.49\,\mathrm{sinc}\left(\frac{2\pi r}{w} + \pi\right) + 0.49\,\mathrm{sinc}\left(\frac{2\pi r}{w} - \pi\right) \quad (2)$$

One may simply substitute linear dimension x for r to represent the linear masks. We have studied masks with IWA ranging from 2.0 λ/D to 4 λ/D. Here the IWA is defined as the point at which the mask has 50% intensity throughput. Table 2 gives the width parameter w and the Lyot throughput for the hybrid radial and linear masks used in the study. These masks have 50% throughput at the stated IWA. The system transmission at the IWA is then ½ of the Lyot transmission (columns 4 and 5 for circular and linear masks, respectively).

Table 2. Complex Mask Width and Lyot Throughput

IWA	w (λ/D)	D_{Lyot}/D_{pupil}	Circ. Trans.	Linear Trans
2	4.329	0.530	0.280	0.610
2.5	5.411	0.610	0.372	0.516
3	6.494	0.672	0.450	0.589
4	8.659	0.751	0.564	0.686

In our previous TPF-C CEB work, we employed 8th order masks. These masks have a broader region of high optical density, have steeper transmission edges, and have superior aberration rejection but much lower Lyot throughput than 4th order masks.[29,30] Unfortunately, they have prohibitively low throughput at 2 λ/D. The combination of 4th order masks and IWA= 2 λ/D results in tolerances that are much tighter in the current work than in our TPF-C work.

2.3 Contrast analysis

All of the system perturbations ultimately result in two sources of coherent scatter: aberrations (including tip/tilt), and beam walk. We express aberrations in terms of Zernike polynomials, and beam walk in terms of sheared spatial frequencies.

Table 3: Coefficients of Aberration Leakage

	I_r		I_a		σ_a	
Zernike	**a**	**p**	**a**	**p**	**a**	**p**
1	0.00E+00	0.00	0.00E+00	0.00	0.00E+00	0.00
2	4.17E-03	3.26	6.16E-08	2.40	3.27E-06	3.09
3	4.17E-03	3.26	6.16E-08	2.40	3.27E-06	3.09
4	5.58E-02	2.00	4.34E-07	1.98	1.27E-07	1.93
5	1.42E-01	3.61	3.77E-05	3.44	2.20E-04	3.79
6	1.42E-01	3.61	4.17E-05	3.45	3.29E-04	3.87
7	2.84E+01	4.15	4.36E-01	2.00	6.71E-01	2.00
8	2.84E+01	4.15	4.36E-01	2.00	6.71E-01	2.00
9	2.43E-01	3.67	3.66E-06	3.02	2.92E-07	2.58
10	2.43E-01	3.67	3.66E-06	3.02	2.92E-07	2.58
11	9.08E-01	2.02	1.63E-07	2.02	1.13E-07	1.99
12	1.15E+01	4.20	9.65E-01	2.00	7.96E-01	2.00
13	1.15E+01	4.20	9.59E-01	2.00	7.88E-01	2.00

We compute the sensitivity to aberrations by propagating individual Zernike aberrations in the pupil through the coronagraph to the image plane assuming an ideal optical system. For circular masks, we analyze the electric fields falling inside 1.2 λ/D wide annuli with the inner edge set to the 50% transmission point of the occulting mask, e.g. for a 2 λ/D mask, the annulus spans 2-3.2 λ/D. We choose this inner edge because smaller radii have growing amounts of low-order scatter and diminishing signal from the planet. The annulus width is set to approximately the equivalent width of the speckles which in turn is well matched to the size of the planet image.

In the case of a radial mask, $M=M(r)$, radial aberrations (e.g. focus, spherical) are transmitted through the system and appear as circularly symmetric rings that are easily distinguished from a planet (Fig. 3). At small aberration levels, the leakage of tip, tilt, astigmatism, and trefoil is almost entirely radial; the azimuthal component becomes relatively more significant as the aberration level grows but is not important for the small wavefront perturbations considered here (e.g. << 0.001 wave) . Of the first 11 Noll-ordered[21] Zernike polynomials, only coma leaks through the circularly symmetric mask and Lyot stop with a strictly azimuthal component. This results in two lobes that are similar in shape to the planet. The azimuthal component of the coherent scatter is the systematic noise floor, while the radial component contributes only to the photometric floor.

We evaluate the radial and azimuthal components within the annuli for each mode j. The radial part of the field $E_j(r,\theta)$ is defined by

$$E_{r,j}(r) = \left(\frac{1}{2\pi}\right)\int_0^{2\pi} E_j(r,\theta)d\theta \qquad (3)$$

and the azimuthal part is the remainder $E_{a,j}(r,\theta) = E_j(r,\theta) - E_{r,j}(r)$. We then compute the radial and azimuthal components of intensity, $I_{r,j} = \left|E_{r,j}(r)\right|^2$, and $I_{a,j} = \left|E_{a,j}(r)\right|^2$. The total intensity is then

$$I = \sum_{j=1}^{n} \left|E_j\right|^2 = \sum_{j=1}^{n} I_{\mathrm{r,j}} + I_{a,j} + 2Re\left(E_{a,j}E_{r,j}^*\right) = I_r + I_a + 2\mathrm{Re}(E_a E_r^*) \ . \quad (4)$$

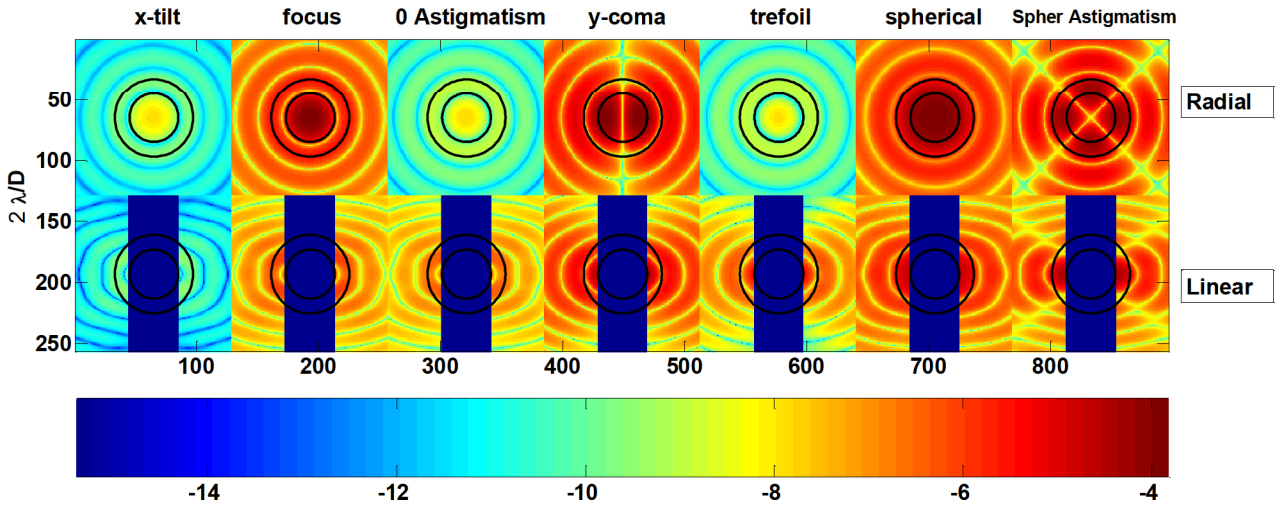

Figure 3. Image plane contrast for low-order Zernike aberrations. Top row: with a circular mask, scatter from tilt, focus, astigmatism, trefoil, and spherical aberration is circularly symmetric (easily distinguishable from a planet image). Scatter from coma and spherical astigmatism (Z13) has lobes that are difficult to distinguish from a planet image. These lobes are amplified when they interfere with the radial aberrations. The two black circles indiate the annulus from 2 – 3.2 λ/D where one would look for a planet centered at 2 λ/D. Internal to this, the scatter grows an the planet signal is dimmed by the opacity of the mask. Bottom row: with a linear mask, the central region +/- 2 λ/D is blocked. Only the arcs on either side contain useful data. The are peaked and difficult to distinguish from a planet image for all aberrations.

Table 3 shows the coefficients a and p of a power law $I = aA_{rms}^{p}$, where A_{rms} is the standard deviation of the aberration in waves fitted to the $I_{r,j}$, $I_{a,j}$, and to the standard deviation $\sigma_{a,j}$ of $I_{a,j}$, within the annulus. The aberration levels used in fitting the power law were 0.0025 and 0.005 waves r.m.s. for each aberration.

In addition to the computation of scatter from aberrations, we also determine the scatter from beam walk. Beam walk is the lateral translation of the light bundle across the optics resulting from motion of an optic or from rigid body pointing motion. The scatter from beam walk is analytically described by the propagation of sheared linear spatial frequencies.[31] The spatial frequency content is derived from power spectral density (PSD) specifications for each optic. These are allocated in the CEB for individual optics in the train except for the deformable mirrors (DMs). The DM PSDs are computed from the root sum square of the PSD of the optics upstream of the coronagraph mask. We assume two DMs, one at the system stop and one about 1 m upstream that is used for broad band amplitude control.[25]
The PSDs of the optics are assumed to follow a power law,

$$PSD = \frac{\mathrm{A}}{1+\left(\frac{\mathrm{k}}{\mathrm{k_O}}\right)^{\mathrm{n}}} \quad (5)$$

such that the PSD is flat at low spatial frequencies $k<k_o$, and rolls off as the nth power at high spatial frequencies. Table 4 shows the parameters used for the telescope and coronagraph optics.

The beam walk analysis[31] does not account for the presence of the coronagraph except to assume that it perfectly removes unaberrated light. We model the effect of the coronagraph by propagating spatial frequencies through the system and observing the leakage inside the aforementioned annular region. This provides a scale factor for the mean

and variance of the scatter for a given amplitude and spatial frequency sine wave. The leaked sine wave amplitude is computed from the PSD and the beam shear, and is proportional to the square of the square of the shear. The shear is determined by the MACOS-generated shear matrix *dB/dx*, where *dB* is the shear on a given optic and *dx* is an allocated motion of a DoF in the system. There is no shear at DM1, the system stop. For any system perturbation *dx*, the chief ray passes through the center of DM1 but may shear on any other optic including the primary mirror.

Table 4. Mirror PSD parameters

Type	D (m)	k_0 (cy/m)	A (m^4)	n	r.m.s. WFE (nm)
pm	3.93	1.02	2E-17	2.5	13.8
sm	0.38	10.61	1E-19	3	8.3
flat	0.06	15.55	6E-22	3	0.7
oap	0.10	9.90	5E-21	3	1.3
dm	0.10	39.60	2E-20	2.5	17.0

2.4 Pointing Control

High precision pointing control is an integral part of the instrument. Pointing control occurs in two stages: a fine steering mirror (FSM) ensures that the stellar image is centered on the coronagraph mask. The FSM is high bandwidth (perhaps several Hz). Rigid body pointing, controlled by reaction wheels, desaturates the FSM and accounts for large amplitude motion (typically several milli-arcsec). Both systems play a role in compensating for pointing errors caused by structural deformation, e.g. due to solar heating of one side of the telescope. Unlike TPF-C, which used an active secondary mirror in the pointing control loop (thus relaxing requirements on the rigid-body pointing limits), the off-axis 3.8 m telescope cannot make use of a tilting secondary mirror because the contrast is much too sensitive to low order aberrations. The pointing control actuators are then the FSM and reaction wheels.

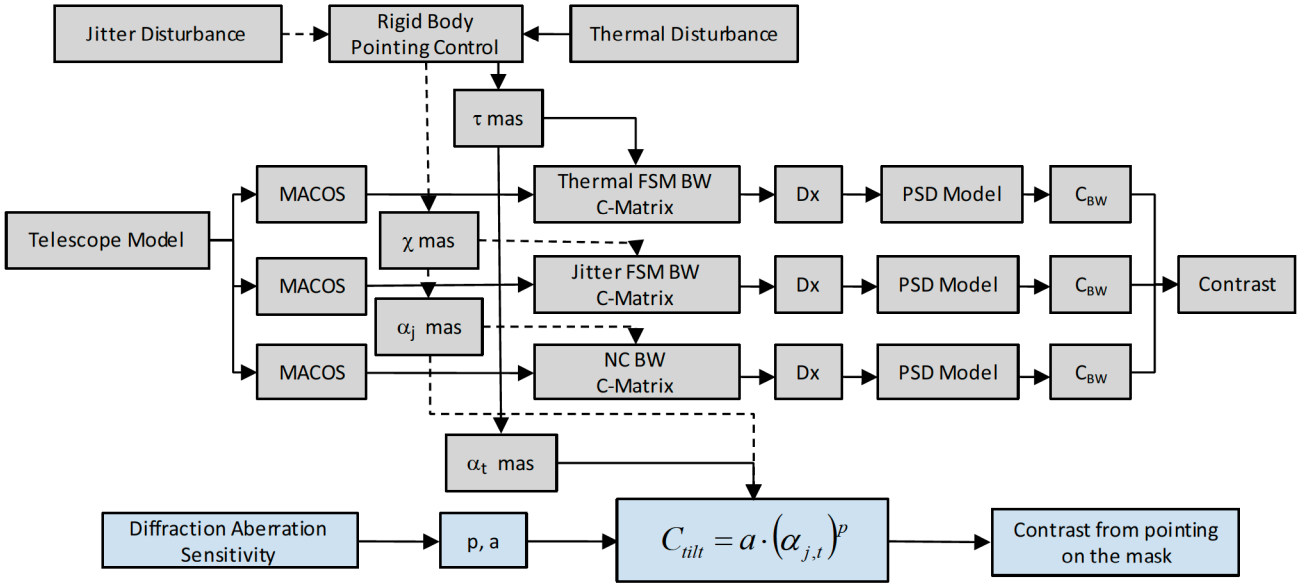

Figure 4. Pointing Control System model.

The optical path through the system depends on which controller is employed. For high frequency jitter, the FSM does not have an adequate sensing signal and has no control authority. Figure 4 shows that there will be some uncompensated rigid body motion with amplitude α_j and that this affects contrast in two ways. First, it leads to beam walk and is evaluated using a MACOS-derived matrix that describes how the beam shears on each optic for strictly rigid body motions. Second, it leads to leakage around the coronagraph mask. This leakage is evaluated using the tip-tilt sensitivities from Table 3. At lower frequency, the FSM controls the light over an angle χ mas. The FSM ensures that the light is centered on the mask, removing beam walk between the pupil and the mask, but leaving unaffected the beam walk from the pupil back to the primary mirror. A separate sensitivity matrix ("Jitter FSM BW C-Matrix" in fig. 4) accounts for this. The CEB allocates the amplitudes of the motions and residuals, and these allocations can be tuned to particular bandwidth regimes once end-to-end modeling is performed on the system.

The pointing system may also suffer two systematic drifts. The zero point of the sensing system drifts relative to the coronagraph mask by an angle α_t. This leads to tip-tilt (Zernikes Z2, and Z3) at the mask and resulting scatter in the image plane. Another systematic drift is the motion of the coronagraph instrument (including DMs and FSM) by τ mas relative to the telescope. This drift is corrected by the FSM and leads to beam walk in the exit pupil. The CEB allocates the allowable drift for both the zero point and the instrument relative to the telescope.

2.5 Wavefront Control System

The CEB assumes that a wavefront control system (WFCS) is employed and consists of: 1) a means of setting the initial contrast to an acceptable value at the start of an observation; and 2) a LOWFS and control system that can monitor and control focus, astigmatism, and coma. We do not model the performance of these systems. We instead allocate a start-of-observation contrast, and we turn on and turn off the low-order Zernike modes to study the requirements with and without the LOWFS.

3. SYSTEMATIC AND PHOTOMETRIC NOISE FLOORS

3.1 Systematic Noise Floor

The image of a planet appears as a faint instrument point-spread function amid coherent speckles and diffraction rings, incoherent instrument background, and zodiacal and exo-zodiacal light. The incoherent scatter and zodiacal light reduce the photometric SNR but do not impose a systematic noise floor. At small working angles, the planet image and speckles are similar in shape; radial spectral smearing of the speckles is negligible over the ~20-30% bandpass used. Speckles are the main cause of the systematic noise floor when radial coronagraph masks are used.. When linear masks (e.g. with transmission function $M=M(x)$) are employed, low-order aberrations manifest as partial diffraction rings in the image plane and these too are difficult to distinguish from the planet image in the low SNR regime as shown in Fig. 3. Partial diffraction rings and speckles together form the systematic noise floor in a coronagraph with a linear mask.

To compute the systematic noise floor for radial masks, we evaluate the variance of the azimuthally dependent intensity in the image plane. We start with the assumption that once the wavefront control system has formed a dark hole, the leaking electric field that reaches the dark hole is small compared to the electric field reaching the coronagraph occulting mask. This allows us to make the approximation that the incident field $E = e^{iS} \approx 1 + iS$. The coronagraph strips off the unaberrated term carried by the '1' and we are left with only the leakage field iS. We can break the leakage field into a static and time-dependent field, and as long as the small angle approximation is valid, they add linearly in the image plane. Thus we begin our analysis by decomposing the electric field at a time t into the sum of a static field, S, present at the start of the observation (after the WFCS has formed the dark hole), and a time-dependent field T that arises as the observation progresses,

$$E(t) = S + T(t) \ . \qquad (6)$$

Following eq. 3, we decompose these fields into their azimuthal and radial components, and for convenience we drop the t but keep in mind that it is implicit in all T terms,

$$E = S_a + S_r + T_a + T_r \quad . \qquad (7)$$

The intensity is then given by

$$\begin{aligned} I &= |E|^2 \\ &= |S_a|^2 + |S_r|^2 + |T_a|^2 + |T_r|^2 \\ &\quad +2\mathrm{Re}(S_a S_r^*) + 2\mathrm{Re}(S_a T_a^*) + 2\mathrm{Re}(S_a T_r^*) \\ &\quad +2\mathrm{Re}(S_r T_a^*) + 2\mathrm{Re}(S_r T_r^*) + 2\mathrm{Re}(T_a T_r^*) \quad . \end{aligned} \qquad (8)$$

We will next isolate the azimuthally varying part of the intensity,

$$I_p = I - |S_r|^2 - |T_r|^2 - 2\mathrm{Re}(S_r T_r^*) \ , \qquad (9)$$

where we have used the subscript p to indicate that this is the systematic noise floor whose behavior mimics the image of a planet. (Note that the term I_a was used in eq. 4 to denote the azimuthal intensity when no radial term is present, thus it does not include the radial/azimuthal interference terms.)

The variance of the systematic noise floor is then given by

$$\sigma_p^2 = \langle I_p^2 \rangle - \langle I_p \rangle^2 \quad . \tag{10}$$

where the expectation is take over temporal variations of the image plane intensity due to mainly to thermal drifts (shot noise is not considered here). To this we must add the initial variance of the azimuthal intensity, $\sigma_{S,a}^2$, to arrive at the total variance of the systematic noise floor

$$\sigma^2 = \sigma_{S,a}^2 + \langle I_p^2 \rangle - \langle I_p \rangle^2 \, . \tag{11}$$

We can express eq. 11 in terms of the mean squared fields in the image plane after first making the assumption that fluctuations in T are zero mean and that the real and imaginary parts are uncorrelated,

$$\langle T_a^R \rangle = \langle T_a^I \rangle = \langle T_r^I \rangle = \langle T_r^I \rangle = \langle T_a^R T_a^I \rangle = \langle T_r^R T_r^I \rangle = \langle T_a^R T_r^I \rangle = \langle T_a^I T_r^R \rangle = 0, \tag{12}$$

with superscripts R and I referring to the real and imaginary parts, respectively. This leads to

$$\begin{aligned} \sigma^2 = \sigma_{S,a}^2 + \sigma_{T,a}^2 + 4\Big(S_a^{R^2} \langle T_a^{R^2} \rangle + S_a^{I^2} \langle T_a^{I^2} \rangle + S_a^{R^2} \langle T_r^{R^2} \rangle + S_a^{I^2} \langle T_r^{I^2} \rangle \Big) \\ + 4\Big(S_r^{R^2} \langle T_a^{R^2} \rangle + S_r^{I^2} \langle T_a^{I^2} \rangle + \langle T_a^{R^2} \rangle \langle T_r^{R^2} \rangle + \langle T_a^{I^2} \rangle \langle T_r^{I^2} \rangle \Big) \quad . \end{aligned} \tag{13}$$

To further simplify the expression, we first consider the nature of the static scatter in the image plane. This scatter exists after the WFCS has iteratively minimized the light to a required level (this level will be examined in Sect. 5). The WFCS controls the amplitude and phase, with equal authority over each. Thus we find that on average the residual light has $S_a^{R^2} = S_a^{I^2}$ and likewise for the radial terms. This allows us to equate

$$4\Big(S_a^{R^2} \langle T_a^{R^2} \rangle + S_a^{I^2} \langle T_a^{I^2} \rangle \Big) = 2 I_{S,a} \langle I_{T,a} \rangle \tag{14}$$

and likewise for the other static/temporal cross-terms.

For the mixing temporal azimuthal and radial terms (the last two terms added in eq. 13) we consider each scatter mode of the field T. These modes originate at phase variations in the telescope pupil; changes in reflectivity and polarization on the timescale of an observation are negligible, as are temporal amplitude fluctuations related to the Talbot effect.[25] The phase modes, in the small angle approximation, are either imaginary/odd or imaginary/even in the pupil. From Table 3 and fig. 4, we see that coma is the main aberration with an azimuthal component. Spherical Astigmatism has an azimuthal component as well but will be much less likely to arise than coma, so it is not considered here. Coma is imaginary/odd, so it will be real/odd in the image plane; for coma, there is a $\langle T_a^{R^2} \rangle$ term but no such imaginary term. There are no other odd azimuthal terms. For the other aberrations, the leakage is predominantly radial. These terms (imaginary/even in the pupil) will be imaginary/even in the image plane, simply $\langle T_r^{I^2} \rangle$. We find then that there are no terms $\langle T_a^{R^2} \rangle \langle T_r^{R^2} \rangle + \langle T_a^{I^2} \rangle \langle T_r^{I^2} \rangle$ and (as long as spherical astigmatism is small compared to the radial terms), the last two temporal cross terms in eq. 14 can be dropped.

Finally, we have

$$\sigma^2 = \sigma_{S,a}^2 + \sigma_{T,a}^2 + 2 I_{S,a} \big(\langle I_{T,a} \rangle + \langle I_{T,r} \rangle \big) + 2 I_{S,r} \langle I_{T,a} \rangle \tag{15}$$

Thus, the scatter that can be confused with a planet is equal to the azimuthal scatter at the start of the observation σ_s^2, plus the scatter arising from temporal changes to the azimuthal component of the electric field, σ_a^2, plus the product of the mean intensities arising from the azimuthal and radial fields, effectively a heterodyning of the static field by the temporal field. Radially symmetric terms such as focus and spherical aberration, and other terms that are, at low aberration levels in the band limited coronagraph, predominantly radial in nature including tip/tilt and astigmatism,

impact the systematic noise floor only through their coherent interference with predominantly azimuthal coma. The implication of eq. 15 is that when a circular coronagraph mask is used, coma, which directly contributes to the systematic noise floor through $\sigma_{r,a}^2$, has a much tighter stability requirement than any of the other low-order aberrations.

The mean and variance terms of eq. 15 depend on the statistics of the aberrations. We are concerned primarily with two cases, linear drift occurring during an observation, and random fluctuations with time constants short compared to an observation. The systematic noise floor is determined by linear drift during the course of an observation (typically several hours), For a linear drift, if we express the instantaneous scatter as $I = aA_{rms}^p$, the mean scatter after a linear drift starting from the ideal state (flat wavefront) and ending at a final aberration level value of A_f is

$$\langle I_t \rangle = \frac{1}{A_f}\int_0^{A_f} aA_{rms}^p dA = \frac{aA_f^p}{p+1} \tag{16}$$

and the variance similarly behaves as

$$\sigma^2 = \frac{a^2 A_f^{2p}}{2p+1} \tag{17}$$

where the values of a and p are found in Table 3 for the azimuthal, radial, and standard deviations of the first 13 Zernike modes. The CEB allocates the maximum amount of drift A_f of an aberration. Functionally, the spreadsheet computes the contrast from Table 3, then applies the correction factors of eq. 16 and 17 to combine the terms together for use in eq. 15.

When a linear mask is used, the central band out to the IWA is obscured. For a planet at the IWA, the light is detectable only in the small fraction of the annulus extending to IWA + 1.2 λ/D (fig. 3). This arc is small and essentially indistinguishable from the light of a planet if one is present. Thus for linear masks, we do not distinguish between radial and azimuthal scatter. Instead, we compute expected mean intensity due to thermal drift using eq. 13, and combine it with the initial combined radial and azimuthal static intensity I_s at the start of the observation. We find that the variance of the intensity in the image plane is then

$$\sigma^2 = \langle I_s \rangle^2 + 2\langle I_s \rangle \langle I_t \rangle \tag{18}$$

as we reported in our earlier work.[13] Aime & Soummer[32] found the same result for pinned speckles. In our case, the initial static intensity constitutes the 'pinned speckles.'

For any aberration with a period short compared to the observation, the interference products in eq. 15 are reduced by N, the number of periods during the observation. It is effectively zero for any mechanical mode of the structure since the observations last for hours (N > 1000). Mechanical modes may contribute a fixed pattern background (e.g. the secondary mirror oscillates slightly around a particular axis, inducing coma), but here we treat the dynamical scatter as azimuthally independent when averaged over the exited mechanical modes. This light contributes to the background photometric noise but not to the systematic noise floor. Assuming these high frequency modes have a Gaussian distribution with standard deviation A_h, modes with p=2 (e.g. focus, beam walk) will have a mean scatter level of $I = aA_h^2$. Modes with other values of p will have a mean value given by the integral of the product of the Gaussian distribution with intensity law $I = aA^p$. These have been evaluated numerically and the appropriate scaling factors are incorporated into the CEB when these terms are combined.

3.2 Photometric Noise Floor

The photometric noise floor is the simple sum of all the radial and azimuthal intensity terms, static and dynamic,

$$\langle I \rangle = \langle I_a \rangle + \langle I_r \rangle + I_i \tag{19}$$

where I_i is the mean contrast level in the evaluation annulus at the start of the observation. The requirement for this floor is that it should not be the limiting noise factor, i.e. it should be no larger than the zodiacal and exozodiacal backgrounds. The CEB presently considers only the coherently scattered starlight. There may be other sources of background as well, e.g. starlight may be multiply scattered into the image plane from baffles or contamination, nearby bright stars may scatter light, or solar glint may be an issue if the sunshade is not properly designed.

4. ERROR BUDGET STRUCTURE AND FUNCTIONALITY

The CEB is a set of excel worksheets including a main budget page, an allocation worksheet, and separate worksheets addressing each type of perturbation (rigid body pointing, flexible body modes, and bending of the optics), each class (aberration and beam walk) and each temporal domain (thermal drift and jitter). The overall structure and methodology including automation is unchanged since we described the CEB in 2009.[14]

There are several important differences between the current CEB and our earlier ones. First, we now calculate the contrast in one of two ways, depending on the choice of coronagraph mask. For radial masks, eq. 15 is used, while for linear masks, eq. 18 is used. We now determine requirements on the amount of linear thermal drift for each parameter, and we compute the coherent scatter of thermal drift separately from the additive scatter of random jitter.

Second, we have added a LOWFS switch that turns off the first 8 Zernike aberrations (with respect to drift; jitter terms are still present) to simulate the effect of perfectly measuring and controlling them with some bandwidth. This allows us to explore the requirements driven by jitter.

Third, we have not yet implemented mask imperfections. In the previous CEB, coronagraph mask errors were a major source of error, and they will be important to simulate in a 4 m class coronagraph as well. However, they are not expected to degrade the performance as severely using the 4th-order masks considered her, compared to the 8th-order masks used in the TPF-C study.

Finally, we have implemented a push-button sensitivity study capability. The tool generates tables of the change in the systematic and photometric noise floors for each allocated parameter, and sorts them from the most to least significant changes. This shows the sensitivity including the coherent combination of all terms, which can be quite different from individual contributions, and allows us to identify the allocations that are the key drivers in the CEB. Table 4 identifies the terms that most significantly affect the contrast with a complex radial mask coronagraph working at 2 λ/D.

Finally, while we carry placeholders for error budget reserve (set uniformly to a factor of 2 in the previous error budget), we have them set to unity here. We do not have any reserve allocated for modeling errors and modeling uncertainties.

5. STABILITY REQUIREMENTS IN A 3.8 M CORONAGRAPH

5.1 Science Requirements Flowdown

There are two key science requirements from which the system stability requirements are derived. First, the faintest planets to be observed are 4 x 10^{-11} times fainter (Δmag = 26) than their host star.[3] Second, the total mean scattered light level should not be brighter than the exozodiacal light, roughly 1 x 10^{-10} time fainter than the host star for exozodi densities equal to our own zodiacal density. The first requirement demands the systematic noise floor have a standard deviation no greater than 10^{-11} in the dark hole for a detection signal-to-noise ratio SNR $\geq$ 4. The second requirement sets the photometric noise floor so that the instrument scatter is not the dominant factor in determining integration time. While more rigorously defined requirements can be put forward (e.g. Kasdin[33]), the requirements to have an SNR $\geq$ 4 against systematic noise and instrument scattered light level no greater than the incoherent background are reasonable starting points. Every factor of 2 change in these requirements is roughly a factor of 1.41 in thermal drift and jitter requirements.

The systematic noise floor consists of the variance of the scatter at the start of the observation plus the variance arising from thermal drift. Combined, these terms must fit within the requirement $\sigma = 10^{-11}$. We have allocated an initial azimuthal contrast standard deviation $\sigma_{S,a}$ = 5x10^{-12}, an initial mean azimuthal and radial contrast levels $I_{S,a}$=$I_{R,a}$ =5x10^{-12}. This allows the thermal drift of the coma and cross terms to add 8.7x10^{-12} (these terms add in quadrature) in contrast.The photometric noise floor is the sum of all the scatter at the start of the observation plus the mean value of the scatter from thermal drift and dynamical jitter. We have allocated an initial mean contrast level of I_i = 10^{-11}, and allow the thermal and dynamical terms to contribute and additional 9 x 10^{-11}. However in the allocation shown in Figure 5, we looked at what happens when dynamic terms are comparable to thermal drift terms and found that the instrument photometric background came up to ~7x10^{-11}. The overall CEB structure is shown in fig. 5.

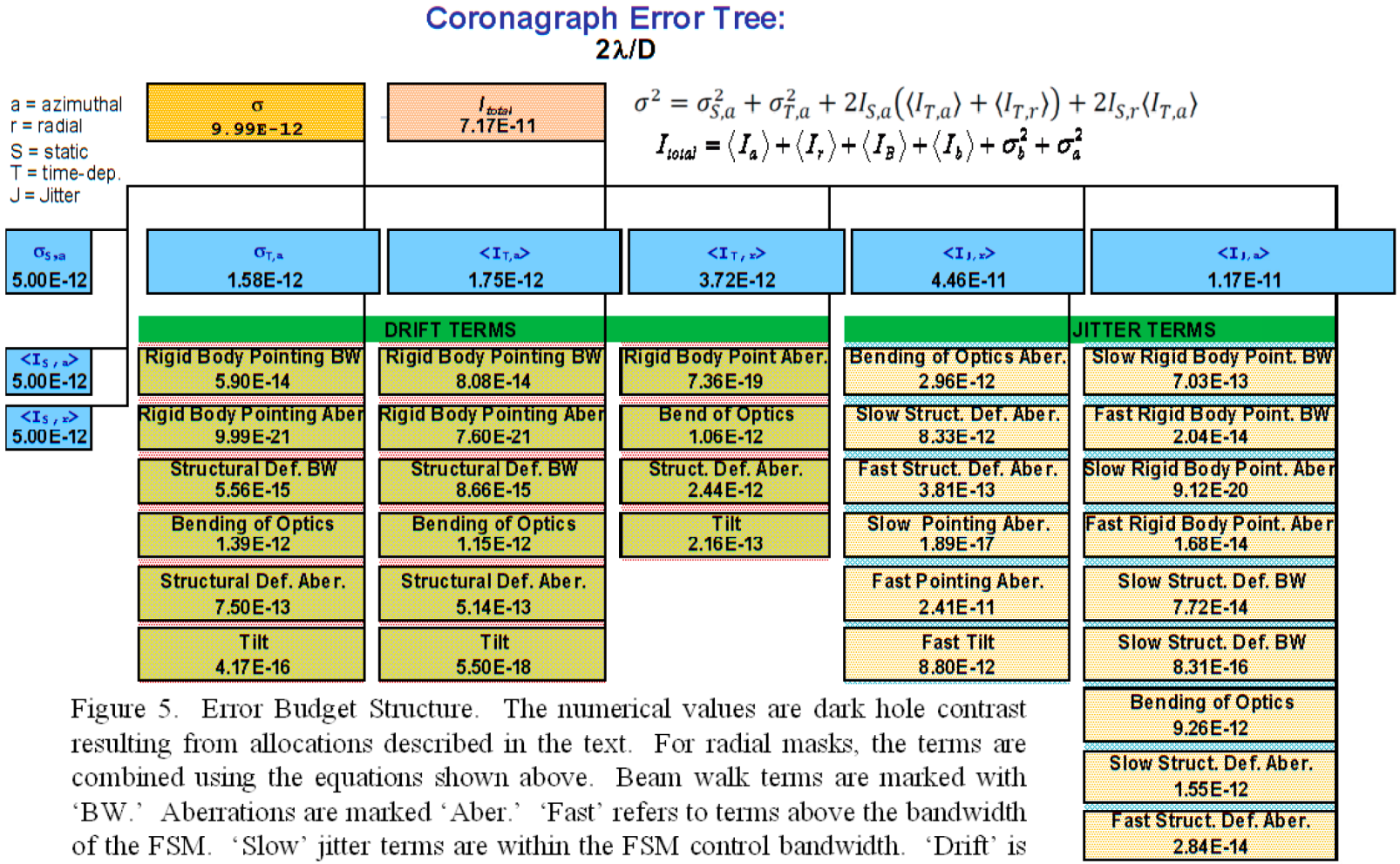

Figure 5. Error Budget Structure. The numerical values are dark hole contrast resulting from allocations described in the text. For radial masks, the terms are combined using the equations shown above. Beam walk terms are marked with 'BW.' Aberrations are marked 'Aber.' 'Fast' refers to terms above the bandwidth of the FSM. 'Slow' jitter terms are within the FSM control bandwidth. 'Drift' is systematic drift over the full observation.

The reader is reminded that the thermal and dynamic allocations discussed below are predicated on the wavefront control system (WFCS) achieving these levels of systematic and photometric noise, $\sigma_{s,a} = 5\text{x}10^{-12}$, and $I_i = 10^{-11}$, respectively, at the start of the observation. The allocations will be tightened if the WFCS does not meet this performance. To date the best performance achieved in the laboratory in 10% broadband light[26] is ~$5\text{x}10^{-10}$, still two orders of magnitude worse than called for here.

5.2 Main Drivers

After an initial allocation, based roughly on the TPF-C error budget, we recognized that there were three extremely challenging areas that demanded the lion's share of the error budget: these are rotational and translational motion of the secondary, bending (particularly coma) of the primary mirror, and pointing control. Table 5 lists the parameters that have been allocated the largest portion of the systematic error budget for detection at 2, 2.5, and 3 λ/D. Columns 2, 4, and 6 give the maximum allowed drift during an observation for the parameters named in column 1. Columns 3, 5, and 7 are the change in contrast if a given parameter drifts by double the allowed maximum. This column takes into account the background and azimuthal cross terms of eq. 15. We have allocated requirements so that PM coma and SM axial drift contribute roughly the same systematic noise. Lateral motion of the secondary is next, followed by spherical aberration of the PM. Also significant is the zero-point offset drift for pointing, PM focus, SM angular drift, and finally drift in the line of sight.

PM bending and SM motion are self explanatory. The bending terms are for the optical wavefront – surface stability requirements are 2 times tighter. The zero-point offset drift is a requirement on the calibration of the pointing system. This term is the registration error of the measured image position relative to the center of the coronagraph mask and it introduces scatter through tip/tilt aberration at the mask. The line of sight drift requirement is the motion of the coronagraph mask relative to the chief ray of the telescope and coronagraph. This drift introduces beam walk, mainly on the fold and focusing optics within the instrument.

Table 5. Key requirements for systematic noise floor, radial masks, at 2, 2.5, and 3 λ/D.

	2 λ/D radial complex		2.5 λ/d radial complex		3 λ/d radial amplitude	
Allocation	Reqmnt.	ΔContrast	Reqmnt.	ΔContrast	Reqmnt.	ΔContrast
PM x-coma drift, picometers	1.00	2.0E-12	2.50	2.0E-12	5.00	2.7E-12
PM y-coma drift, picometers	1.00	2.0E-12	2.50	2.0E-12	5.00	2.7E-12
Secondary Mirror z-motion drift, nm	0.40	1.9E-12	0.80	2.0E-12	1.60	1.8E-12
Secondary Mirror y-motion drift, nm	0.80	1.7E-12	1.60	2.0E-12	3.00	1.4E-12
PM spherical aberration drift, picometers	1.00	1.1E-12	2.00	1.3E-12	4.00	4.8E-13
Secondary Mirror x-motion drift, nm	0.80	7.6E-13	1.60	4.1E-13	3.00	6.1E-13
Pointing zero-point x-offset drift, milliarcsec	0.10	4.5E-13	0.14	6.4E-13	0.30	7.5E-13
Pointing zero-point y-offset drift, milliarcsec	0.10	4.5E-13	0.14	6.4E-13	0.30	7.5E-13
PM focus drift, picometers	2.00	3.7E-13	4.00	4.9E-13	8.00	3.3E-13
Secondary Mirror x-tilt drift, milliarcsec	0.17	2.6E-13	0.34	1.4E-13	0.62	2.2E-13
Secondary Mirror y-tilt drift, milliarcsec	0.17	2.2E-13	0.34	1.2E-13	0.62	1.9E-13
Line-of-sight x-drift, milliarcsec	2.00	1.5E-13	2.00	2.2E-13	2.00	2.8E-13

Table 5 shows that for detection at 2 λ/D using a radial mask, the requirements on PM coma, spherical aberration, and focus drift are 1, 1, and 2 picometers per observation. The observations may last from minutes to days depending on the brightness of the star and the desired contrast depth. The requirements for secondary mirror drift are 0.4 nm in focus, 0.8 nm in both lateral dimensions and 0.8 nrad (0.17 mas) in tilt. The zero point drift of the pointing system is 0.1 mas, while the drift of the line of site relative to the mask is 2 mas.

Moving to 2.5 λ/D, the requirements are relaxed by a factor of 2 in most cases. They relax another factor of 2 at 3 λ/D. At 3 λ/D, the radial amplitude-only mask is more tolerant of aberrations than the complex mask having the same half-power width. This is because the phase term in the complex mask leads to more pronounced ringing of the aberrations and this effect is significant at 3 λ/D.

There are many other allocated drift parameters in the systematic error budget, including bending requirements on all optics, and positional stability requirements on all optics. For bending, we assume that the SM bends ¼ as much as the primary (thus, SM coma is allowed to drift by 0.25 pm for 2 λ/D observations), and the downstream optics are assumed to bend 1/8 as much as the PM. For all optics following the secondary mirror, the positional drift is allocated 10 nm and 10 nrad. These values can be relaxed a factor of a few (but not by an order of magnitude) without having a major impact on performance. However, since we have sub-nm requirements on the secondary mirror, it is reasonable to assume that 10 nm requirements on the instrument positional stability are readily achieved.

The instrument photometric noise floor (eq. 19) is the sum of all the intensity contributions including static, drift, and jitter (but not including multiple-scatter sources such as veiling glare due to dust or originating other than from the target star). The key requirements are summarized in Table 6 for IWA = 2 λ/D. The requirements listed in the table are the standard deviation of the motion for those labeled 'jitter' and the full amplitude of the drift for those labeled 'drift.' The latter are the same terms appearing in Table 5. When the parameters are limited to the values of Table 6, column 2, the instrument mean contrast is $7x10^{-11}$. Column 3 of Table 6 shows the change in mean contrast when the parameter change is double the allocated amount. As with the systematic noise allocations, we have attempted to give the largest pieces of the photometric contrast budget to what we expect to be the most challenging aspects of the design.

Table 6. Key requirements for photometric noise floor.

	2 λ/D radial complex	
Allocation	Reqmnt.	ΔContrast
Secondary Mirror z-motion, slow jitter, nm	1.0	7.8E-11
Secondary Mirror y-motion, slow jitter, nm	1.5	3.4E-11
PM spherical aberration jitter, picometers	2.0	2.7E-11
PM x-coma jitter, picometers	2.5	2.7E-11
PM y-coma jitter, picometers	2.5	2.7E-11
Rigid body pointing, high-freq, y-axis, milliarcsec	0.1	1.5E-11
Rigid body pointing, high-freq, x-axis, milliarcsec	0.1	1.5E-11
PM x-spherical astigmatism jitter, picometers	1.0	9.6E-12
PM y-spherical astigmatism jitter, picometers	1.0	9.5E-12
PM focus jitter, picometers	4.0	9.0E-12
Secondary Mirror x-motion slow jitter, nm	1.5	6.6E-12
Secondary Mirror z-motion drift, nm	0.4	4.2E-12
Secondary Mirror y-motion drift, nm	0.0	3.3E-12
Secondary Mirror x-tilt slow jitter, milliarcsec	0.3	2.4E-12
PM spherical aberration drift, picometers	1.0	2.2E-12
Secondary Mirror y-tilt slow jitter, milliarcsec	0.3	2.1E-12
PM x-coma drift, picometers	1.0	1.4E-12
PM y-coma drift, picometers	1.0	1.4E-12

The jitter parameters are divided into three categories. Those labeled 'slow jitter' produce aberrations including tip/tilt (Zernike modes 2 and 3). 'Slow' indicates that the FSM is correcting Z2 and Z3 so that only higher order aberrations and beam walk contribute to the change in image plane contrast. "High-freq" jitter is motion beyond the FSM bandwidth. We do not determine what the bandwidth is (this depends on the instrument design and target brightness), but allocate an allowable uncompensated contrast loss. Terms simply labeled 'jitter' do not introduce tip-tilt and are not controlled.

The secondary mirror jitter is allocated 1 nm r.m.s. of slow jitter in the z-axis and 1.5 nm in the x and y axes. The PM jitter mode allocations are 2 pm of spherical aberrations, 2.5 pm of coma (each axis), 1 pm of spherical astigmatism, and 4 pm of focus. The high-frequency rigid body pointing residual is 0.1 milli-arcsec. Lower-frequency rigid body pointing (sufficiently slow to be controlled by the FSM) is allocated 4 mas/axis and contributes contrast from beam walk that is $\sim 10^{-12}$. Several drift terms are also significant contributors; these are limited by their contributions to the systematic noise floor.

Table 7. Key requirements for linear mask systematic noise floor.

	2 λ/D linear complex	
Allocation	Reqmnt.	ΔContrast
Secondary Mirror z-motion drift, nm	0.50	2.6E-12
Secondary Mirror y-motion drift, nm	1.00	2.3E-12
PM y-coma drift, picometers	1.50	1.9E-12
Pointing zero-point x-offset drift, milliarcsec	0.12	1.3E-12
Pointing zero-point y-offset drift, milliarcsec	0.12	1.3E-12
PM focus drift, picometers	4.00	1.3E-12
PM spherical aberration drift, picometers	1.00	1.2E-12
Line-of-sight x-drift, milliarcsec	2.00	1.2E-12
PM x-coma drift, picometers	3.00	7.0E-13
PM 0-astigmatism drift, picometers	4.00	6.4E-13
Secondary Mirror x-motion drift, nm	1.00	6.0E-13
PM x-trefoil drift, picometers	2.00	3.9E-13
PM x-trefoil drift, picometers	2.00	3.1E-13
Secondary Mirror y-tilt drift, milliarcsec	2.00	1.9E-13

We note that the finite diameter of the stars will add background at small IWA. A star with angular radius 0.5 mas (the Sun at 10 pc) will contribute a background scatter of 2.3×10^{-11} for IWA = 2 λ/D. A solar type star at 6 pc adds 1.1×10^{-10}. The leakage is reduced to 3.7×10^{-11} at 2.5 λ/D for a star at 6 pc.

The key requirements for a linear complex mask at 2 λ/D are shown in Table 7. The linear mask has a larger Lyot opening than the corresponding radial mask which confines the diffraction rings from aberrations to smaller radii where they have less impact compared to the radial mask. This affords some relaxation of requirements, e.g. coma drift relaxes from 1.0 pm for the radial complex mask compared to 1.5 pm for the linear complex mask, while focus relaxes from 2 to 4 pm, respectively. On the other hand, the leaking diffraction arc segments are largely indistinguishable from the light of a planet, so the system is directly sensitive to all low order aberrations, not just the ones with azimuthal leakage. This calls for single-digit picometer requirements on astigmatism and trefoil in addition to focus, coma, spherical aberration, and spherical astigmatism. Requirements relax at 2.5 and 3 l/D similarly to the radial mask in Table 5. Photometric noise floor performance is similar to Table 6.

5.3 Requirements with a LOWFS

As noted in Sect 4, the LOWFS is assumed to provide perfect measurement of the first 8 Zernike aberrations (tip, tilt, focus, 0 and 45 astigmatism, x and y coma) within some bandwidth. The bandwidth is assumed to be sufficient to track the linear drift terms, but insufficient for any jitter terms. This is different from the FSM which is assumed to have sufficient bandwidth to track the 'slow' jitter terms. The assumption here is that the LOWFS isn't adequate to track these 'slow' terms which may in fact be as fast as several Hz. Further, the LOWFS must maintain its calibration over the full observation. For example, while it may be possible to sense and control the low-order aberrations on timescales of a few minutes, the LOWFS must maintain its picometer coma and focus calibration for the full period of the observation which may be many hours.

The LOWFS is implemented by turning off the thermal drift Zernike aberrations. The x and y coma drift are the main contributors to the systematic noise floor without the LOWFS (Table 6) but they are absent here as is focus drift. Table 8 shows the key requirements with the LOWFS in place. Several parameters have been significantly relaxed because of the LOWFS. PM Focus, astigmatism, and coma drift are set to 1.5 nm (compared to single-digit picometers in Table 6). They could be further relaxed if necessary. Secondary mirror drift is also significantly relaxed to 15 nm lateral and 10 nm axial, compared to 0.8 and 0.4 nm, respectively, without the LOWFS. Other parameters are slightly, or not relaxed. Spherical aberration drift is 2 nm, and spherical astigmatism drift is 0.2 pm. It is allocated less amplitude than spherical aberration because it is less likely to be induced by thermal deformation of the primary. The zero-point drift of the pointing system has been relaxed by a factor of 2 to 0.2 mas.

Table 8. Key requirements for radial complex mask systematic noise floor, with LOWFS.

	2 λ/D radial complex	
Allocation	Reqmnt.	ΔContrast
PM spherical aberration drift, picometers	2.00	3.8E-12
Pointing zero-point x-offset drift, milliarcsec	0.20	3.7E-12
Pointing zero-point y-offset drift, milliarcsec	0.20	3.7E-12
Secondary Mirror x-motion drift, nm	15.00	1.1E-12
Secondary Mirror y-motion drift, nm	15.00	1.1E-12
Secondary Mirror z-motion drift, nm	10.00	5.9E-13
Secondary Mirror y-tilt drift, mas	3.00	3.4E-13
Secondary Mirror x-tilt drift, mas	3.00	3.3E-13
Line-of-sight x-drift, milliarcsec	2.00	1.4E-13
PM spherical astigmatism drift, picometers	0.20	1.3E-13
Line-of-sight y-drift, milliarcsec	2.00	9.5E-14

The photometric noise floor requirements (Table 9) are similar with and without the LOWFS because they are mainly driven by jitter. Allowable PM jitter of coma has been reduced to 2 pm (from 2.5) with the LOWFS to accommodate the increased contributions of aberration and other low-order aberrations (e.g. the 15 nm coma thermal drift shows up at the bottom of Table 9). Other PM jitter terms remain at single-digit picometers.

6. CONCLUSION

Several key requirements presented here for an aggressive 2 λ/D coronagraph on a fast, off-axis 3.8 m telescope are 1-2 orders of magnitude tighter than the corresponding requirements for TPF-C. For example, the TPF-C PM bending

modes were allocated 200-400 pm, and the secondary mirror was allocated 65 nm lateral and 25 nm axial motion. The pointing calibration offset was 0.3 mas, compared to a 0.1 mas allowable drift in the present work. (An apples-to-apples comparison is not possible for all terms since we have changed the way certain parameters are allocated.) There are two main reasons for this dramatic increase in sensitivity to bending and motion. First, the requirement to work at 2 or 2.5 λ/D means that the detection annulus is sensitive to the core of the scatter lobe from low-order aberrations. Second, a 4th-order band-limited mask is required (or similar coronagraph with 4th order, or higher, near-axis behavior) because higher order masks need small Lyot stops that have virtually no throughput and wide diffraction lobes in the image plane. Unlike the 8th-order masks, 4th-order masks do not filter the low-order aberrations.[29]

Table 9. Key requirements for photometric noise floor, with LOWFS.

	2 λ/D linear complex	
Allocation	Reqmnt.	ΔContrast
Secondary Mirror z-motion, slow jitter, nm	1.0	7.8E-11
Secondary Mirror y-motion, slow jitter, nm	2.0	6.1E-11
PM x-coma jitter, picometers	2.0	1.7E-11
PM y-coma jitter, picometers	2.0	1.7E-11
Rigid body pointing, high-freq, y-axis, milliarcsec	0.1	1.5E-11
Rigid body pointing, high-freq, x-axis, milliarcsec	0.1	1.5E-11
Secondary Mirror x-motion slow jitter, nm	2.0	1.2E-11
PM x-spherical astigmatism jitter, picometers	1.0	9.6E-12
PM y-spherical astigmatism jitter, picometers	1.0	9.5E-12
PM spherical aberration drift, picometers	2.0	9.1E-12
PM focus jitter, picometers	4.0	9.0E-12
Line-of-sight x-drift, milliarcsec	2.0	8.9E-12
Line-of-sight y-drift, milliarcsec	2.0	8.9E-12
PM spherical aberration jitter, picometers	1.0	6.7E-12
Secondary Mirror x-tilt slow jitter, milliarcsec	0.4	4.3E-12
Secondary Mirror y-tilt slow jitter, milliarcsec	0.4	3.7E-12
Secondary Mirror y-motion drift, nm	15.0	1.7E-12

In fact, this is precisely why TPF-C was designed with an 8 m long PM and a deployed SM – with this combination it achieved an adequate IWA and throughput at 4 λ/D using and 8th-order mask, and this allowed the telescope requirements to relax within what appeared to be a reasonable set of engineering requirements. Thermal and dynamics models showed that TPF-C could be built to meet the requirements of the stability error budget.[3]

Here we see that the coronagraph will drive many of the engineering requirements on an astrophysics mission. Whereas the astrophysics calls for an on-axis, diffraction limited telescope, the coronagraph requires an off-axis telescope with extraordinary stability requirements and unprecedented pointing control. These in turn requires a sophisticated thermal control system, high-precision metrology to the secondary mirror, and sub-nm positional control systems. There may be other constraints such as sun pointing angles and roll requirements that impact the astrophysics operation. Further, the coronagraph is sensitive to polarization from the large off-axis angles that may require dielectric coatings that impact the minimum wavelength transmitted by the telescope (see Balasubramanian *et al*, this conference[34]).

A LOWFS affords substantial relaxation of the most challenging requirements, perhaps to within readily achievable levels. The requirement on the LOWFS is to achieve a sensitivity of ~5e-12 for drift of focus, astigmatism, and coma while maintaining the start-of-observation calibration for the duration of the observation period. Research in this area should be actively pursued. Even with the LOWFS, however, the SM jitter requirements are 1-2 nm, and PM bending due to jitter is in the single-digit picometer realm.

As daunting as the requirements may appear to be, one should not lose sight of the accomplishments in the laboratory and relate them back to the telescope requirements. Experiment on the HCIT testbed have achieved and maintained better than 10^{-9} contrast[27] in dark holes from 4-10 λ/D. This implies a wavefront stability of ~5 pm at any spatial frequency within the dark hole. While this is only the instrument, not the full telescope, it does show that a complex optical system has achieved single-digit picometer level stability, and at the very least, instruments exist with the sensitivity to test mirror stability to these levels.

We would like to acknowledge helpful discussions with Dwight Moody, John Trauger, and Brian Kern. This work was carried out at the Jet Propulsion Laboratory, California Institute of Technology, under contract to the National Aeronautics and Space Administration.

REFERENCES

[1] 2010 Science Plan for NASA's Science Mission Directorate, National Aeronautics and Space Administration (July 2010). Available at http://science.nasa.gov/media/medialibrary/2010/08/10/2010SciencePlan.pdf .

[2] Committee for a Decadal Survey of Astronomy and Astrophysics; National Research Council, "New Worlds, New Horizons in Astronomy and Astrophysics," ISBN: 0-309-15800-1 (2010).

[3] Levine, M., Shaklan, S. B., & Kasting, J., eds, "Terrestrial Planet Finder Coronagraph, Science and Technology Definition Team (STDT) Report," JPL Document D-34923, available at http://planetquest.jpl.nasa.gov/TPF/STDT_Report_Final_Ex2FF86A.pdf (2006).

[4] Trauger, J. (PI), "ACCESS, A Space Coronagraph Concept For Direct Imaging and Spectroscopy of Exoplanetary Systems," available at http://exep.jpl.nasa.gov/files/exep/ACCESS_Compiled_Report_Public_090610.pdf (2009)

[5] Trauger, J., *et al*., "ACCESS – a NASA mission concept study of an Actively-Corrected Coronagraph for Exoplanet System Studies," Proc. SPIE 7010, 701029-1 (2008).

[6] Guyon, O., *et al*., "The pupil mapping exoplanet coronagraphic observer (PECO)," Proc. SPIE 7731, 773129 (2010).

[7] Clampin, M. (PI), "The Extrasolar planetary Imaging Coronagraph: Architectures of Extrasolar Systems, ASMC Study Report," available at http://exep.jpl.nasa.gov/files/exep/ASMC-Clampin.pdf (2009).

[8] Shao, M. (PI), "An Astrophysics Strategic Mission Concept Study Dilute Aperture Visible Nulling Coronagraph Imager (DaViNCI), Imaging and Spectroscopy of Exo-planets from Nearby Stars," available at http://exep.jpl.nasa.gov/files/exep/DAViNCI_ASMCS_Report-external-2011-04-07.pdf (2011).

[9] Postman, M. (PI), "Advanced Technology Large-Aperture Space Telescope (ATLAST): A Technology Roadmap for the Next Decade," available at http://exep.jpl.nasa.gov/files/exep/ATLAST_NASA_ASMCS_Public_Report.pdf (2009).

[10] Spergel, D. N. (PI), THEIA ASMCS Documentation, available at http://www.astro.princeton.edu/~dns/theia.html (2009).

[11] Cash, W. (PI), "Final Report Astrophysics Strategic Mission Concept Study, The New Worlds Observer," available at http://newworlds.colorado.edu/documents/ASMCS_Report/nwo_main.pdf (2009).

[12] Shaklan, S. B, *et al*., "A starshade petal error budget for exo-earth detection and characterization," Proc. SPIE 8151 (this conference, 2011).

[13] Shaklan, S. B., *et al.*, "The Terrestrial Planet Finder Coronagraph Dynamics Error Budget," Proc. SPIE 5905, 59050D-1 (2005).

[14] Marchen, L., & Shaklan, S., "A general tool for evaluating high-contrast coronagraphic telescope performance error budgets," Proc. SPIE 7440, 74400V1-12 (2009).

[15] Shaklan, S. B., *et al*., "Error Budget and Tolerancing of Starshades for Exoplanet Detection," Proc. SPIE 7131, 71312G (2010).

[16] Guyon, O., Matsuo, T., & Angel, R., "Coronagraphic low-order wave-front sensor: principle and application to a phase-induced amplitude coronagraph," Ap. J., 693, 75-84 (2009).

[17] Green, J. J., & Shaklan, S. B., "Optimizing coronagraph designs to minimize their sensitivity to low-order optical aberrations," Proc. SPIE 5170, 25 (2003).

[18] Kuchner, M. J., & Traub, W. A., "A coronagraph with a band-limited mask for finding terrestrial planets," Ap. J., 570, 900-903 (2002).

[19] MACOS (Modeling and Analysis of Controlled Optical Systems) Manual, JPL Document.

[20] Krist, J. E., "PROPER: an optical propagation library for IDL," Proc. SPIE 6675, 66750P (2007).

[21] Noll, R., J., "Zernike polynomials and atmospheric turbulence," JOSA, 66, 207-211 (1976).

[22] Shaklan, S. B., *et al*., "Terrestrial Planet Finder Coronagraph (TPF-C) White Paper for the NASA-NSF Exoplanet Task Force," available at http://exoplanets.jpl.nasa.gov/documents/TPFC-WhitePaper2-shaklan.pdf (2007).

[23] Scowen, P. A., *et al*, "Design and implementation of the NUV/optical widefield Star Formation Camera for the Theia Observatory," Proc. SPIE 7731, 77314Y (2010).

[24] Kasdin, N. J., "THEIA Telescope for Habitable Exoplanets and Interstellar/Intergalactic Astronomy," White Paper submitted to NRC ASTRO-2010 Survey, available at http://www.astro.princeton.edu/~dns/Theia/nas_theia_v14.pdf (2010).

[25] Shaklan, S. B., & Green, J. J., "Reflectivity and optical surface height requirements in a broadband coronagraph. 1. Contrast floor due to controllable spatial frequencies," Appl. Opt 45, 5143-5153 (2006).

[26] Moody, D. C., & Trauger, J. T., "Design and demonstration of hybrid Lyot coronagraph masks for improved spectral bandwidth and throughput," Proc. SPIE 7010, 70103P (2008).
[27] Kern, B., Kuhnert, A., & Trauger, J. T., "Exoplanet Exploration Program Technology Milestone #2 Report," JPL Document D-60951, available at http://exep.jpl.nasa.gov/files/exep/HCIT-Milestone2Signed-2008-08-08.pdf (2008).
[28] Trauger, J. T., personal communication (2011).
[29] Kuchner, M. J., Krepp, J., & Ge, J., "Eighth-order coronagraph masks for terrestrial planet finding," Ap. J., 628, 466-473 (2005).
[30] Shaklan, S. B., & Green, J. J., "Low-order aberration sensitivity of eighth-order coronagraph masks, " Ap. J., 628, 474-477 (2005).
[31] Noecker, C., "TPF coronagraph wavefront changes due to beam walk," Proc. SPIE 5905, 59050F-1 (2005).
[32] Aime, C. & Soummer, R., "The usefulness and limits of coronagraphy in the presence of pinned speckles," ApJ 612:L85-88 (2004).
[33] Kasdin, N. J., & Braems, I., "Linear and Bayesian planet detection algorithms for the Terrestrial Planet Finder," Ap. J., 646, 1260-1274 (2006).
[34] Balasubramanian, K., *et al*., "Deep UV to NIR Space Telescope and Exoplanet Coronagraphs: a trade study on throughput, polarization, mirror coating options and requirements," Proc. SPIE 8151 (this conference, 2011).